Construction and Building Materials 379 (2023) 131109

Contents lists available at ScienceDirect

Construction and Building Materials

journal homepage: www.elsevier.com/locate/conbuildmat

# Acquiring the size distributions of the aggregates using percolation modeling

Asghar Aryanfar [a,b,*], Maria N. Khoury [a], Irem Şanal [b], Dana Şeyhibrahim [c], Jaime Marian [d]

[a] American University of Beirut, Riad El-Solh, Beirut, 1107, Lebanon
[b] Bahçeşehir University, 4 Çırağan Cad, Beşiktaş, Istanbul, 34349, Turkey
[c] Yıldız Technical University, Davutpaşa Cad, Esenler, Istanbul, 34220, Turkey
[d] University of California, 400 Westwood Plaza, Los Angeles, CA, 90095, USA

ARTICLE INFO

*Keywords:*
Aggregates
Sieve analysis
Image processing
Percolation

ABSTRACT

The recent computation-based image processing techniques the granular aggregates for attaining the size histograms could be a versatile and efficient alternative to the conventional sieve analysis tests, which demand laboratory equipments. Herein a new percolation-based framework is developed for acquiring such particle size distribution which pertains distinctive advantages relative to the recent techniques. Starting with the local binarization of the given cluster of aggregates, the connected chains have been identified by means of percolation and the internal aggregates have been discerned via minimizing the propagation flux and maximizing the roundness in global and local scales respectively. The method is verified via correlating with the experimental gradation, where the higher accuracy versus the conventional binarization is achieved and justified and the correlation with the corresponding resolution is addressed. The developed framework could be utilized as a fast and versatile method for determining the aggregate size distribution in any given granular medium, particularly those of containing irregular and random geometries pertaining sharp corners.

## 1. Introduction

Aggregates form the constituents of many large-scale media such as soil [1], concrete [2], powders [3] as well as agricultural products including rice, beans, etc [4]. Particularly it forms 60%–75% of a typical concrete [5] by volume, hence their size distribution, type and quality largely determine the ultimate physical and mineralogical properties of the concrete [6].

The aggregates analysis includes acquiring shape, texture, size and moisture content, which determines the permeability of the concrete, and combined with the water/cementitious material ratio, controls its ultimate strength, workability, and durability [7–10].

Regarding the analyzing the aggregate, sieving is a popular method used in laboratories and industrial processes to distinguish aggregate particles relative to their sizes [11–14]. It represents the obtained aggregate sizes in cumulative curves based on the aggregate weights between two consecutive sieves [14,15].

Industrial particle separation using sieves is one of the simplest, yet accurate technique for very short 50 μm − 2 mm (i.e. dust/powder) [16]. Although sieving is a well-established technique, it contains a degree of uncertainty since whether a particle will pass a given sieve is dependent upon its instantaneous orientation and cross sectional shape it lacks measurement of any of its axial dimension [17,18].

Several image processing techniques have been applied for computing the properties of concrete aggregates [19–23]. The most commonly encountered problems in aggregates analysis include defining an error threshold or precision value to the algorithms used for determining how to convert areas into masses, since data obtained from images are 2D and data from the sieve analysis are 3D [24], particularly for stress computations [25]. Previous studies presented a visual comparison of curves obtained from sieve analysis and image analysis and proposed different techniques of conversion of areas into masses [17,26–28]. In this context, the projection of size and distribution in the 3rd dimension (i.e. depth) is performed via assumption of the similar patterns of planar observation, which could vary based on the application [29,30]. As well, used two directional (horizontal and vertical) sectional images have been used to increase the prediction accuracy [21].

As well, the mass and volume have additionally been estimated by flakiness measure [31]. Other past works include approximating the critical sieving diameter known as mesodiameter [16], aggregate scale [15] and larger scale [32] analysis.

Other prominent image processing methods have studied the aggregates sizes and distribution using fast and low-cost software. Particularly ImageJ has been utilized to measure the shape parameters of sand aggregates, including the ferret size $F$ and circularity $C$ [33,34], and analyzes the particle size distribution via enclosing them within

* Corresponding author at: American University of Beirut, Riad El-Solh, Beirut, 1107, Lebanon.
*E-mail address:* aryanfar@caltech.edu (A. Aryanfar).

https://doi.org/10.1016/j.conbuildmat.2023.131109
Received 2 January 2023; Received in revised form 25 February 2023; Accepted 18 March 2023
Available online 3 April 2023
0950-0618/

the ellipses of major and minor axis. Such approximation with elliptic form has been explored in a separate study in 2D [34], and 3D aggregates [30,35]. Furthermore, there has been continuous efforts throughout the past decades to develop measures for computing the convexity, sphericity, and aspect ratio from digital images [36–38].

Needless to mention that ImageJ provides more geometrical measures such as reciprocal aspect ratio, rectangularity and feret effect [39], particularly by utilization of tools such as dilate, fill holes and skeletonization [40,41]. Other methods include Glow-in-the-Dark [42], noise removal [43], contrast adjustment [44], image segmentation [27], advanced thresholding for Otsu's binarization and Canny's edge detection [45], determining the third dimension from the standard 2D images [46].

Other methods, such as laser diffraction and single particle optical sizing have been proposed [36]. While the imaging-based aggregate size detection techniques has proven time and accuracy privileges over traditional sieving method, their barrier is the inability of single camera-lens systems to capture the wide range of aggregate sizes in soil [32], and there is still need for standardization of the error [47].

In fact, image processing has been utilized in the broader number of fields, such as detecting aggregates such as rice and beans [48], where it helps evaluating the quality of the crops. In this regard, the machine learning algorithms could enhance characteristic extraction from $2D$ images [49], for achieving higher accuracy [50,51].

However, the image processing techniques has not been enriched enough to accurately address the sieve analysis diagrams yet [27]. Additionally, the complexity of their technique has limited its applicability [36] and more computational improvement is needed.

Percolation theory has long been used to study the behavior of systems with interconnected elements. It has been used in a wide range of disciplines such as transport in porous media [52,53], morphology and fracture of composite materials [54–56], underground hydrodynamic flows [57,58], fractal dispersion, reaction kinetics, and biological systems [59]. The formation of random media expands from connection trees [60–62] and 2D lattices [63–65] to multidimensional continuous particles [66,67], which empowers the percolation theory to predict the emergence of highly connected clusters in stochastic domains [68–70]. It is particularly deals with a certain threshold where a global scale of connectivity is stablished [71,72].

In this paper, a new percolation-based technique has been developed which iteratively minimizes the percolation flux in the larger regions and maximizes the circularity (i.e. roundness) in the smaller sub-regions to identify the optimized estimation from the aggregates and measure their equivalent geometric properties such as area and diameter. The role of the image resolution (i.e. compression factor) on the precision of the aggregate size distribution has been explained, the higher correlation of method with the experiments compared with the Otsu's binarization has been illustrated. The developed methodology could be used for estimating the size distribution in the given medium, particularly for those of irregular shapes and sharp corners.

## 2. Experimental

Five samples of aggregates mixes have been utilized with the total weight of $\approx$ 500 g, sample of each is shown in Fig. 1(a), with the color distribution of Red, Green and Blue. Each set has a different fineness modulus (FM) as given in the Table 1. Next, sieve analysis was performed on each set using Standard sieving method (TS EN 933-1, 2012) [73] by placing the aggregates on the top-most sieve and letting the sieves vibrate for 5 minutes. After the vibration period was over, the mass retained on each sieve was recorded, as visualized in Fig. 1(b). As well the cumulative passing weight percentage was calculated.

Subsequently, image capturing was done on the aggregate mixes. The aggregates were placed on white, non-reflecting paper with a ruler on the side to provide the scale needed for measurements in image analysis, and a camera was placed at a constant height of 30 cm above the aggregates. Two white light lamps were placed around the setup to provide better and clearer images. The lights placement was adjusted to minimize the shadow effect. The aggregates were placed as flatly as possible on the paper surface to avoid overlap due to stacking.

**Table 1**
Experimental parameters.

| Sample no. | 1 | 2 | 3 | 4 | 5 |
|---|---|---|---|---|---|
| $FM$ | 6.36 | 5.93 | 4.62 | 5.44 | 5.04 |

Consequently, a calibration factor was calculate to relate real dimension with the image dimension as below:

$$\alpha = \frac{\text{Scale of the Ruler (m)}}{\text{Image Dimension (pixels)}} \approx 3.75 \times 10^{-5} \frac{\text{m}}{\text{pixels}}$$

## 3. Methodology

The extraction of the aggregates in a bare image is typically challenging. As an example, Fig. 1(a) could get binarized via adaptive thresholding, [74] as shown in the Fig. 2(a). Subsequently the cluster of isolated aggregates could get extracted by means of percolation, as illustrated in Fig. 2(b). Since the aggregates are excessively connected unrealistically, more recognition treatments are needed to get more appropriate aggregate shape size distributions. Herein we define two appropriate variables for further identification of the aggregates from each other, as below:

### 3.1. Propagation flux $\delta A$

We perform percolation on the identified aggregate cluster $n$ through the first-order neighbors (left $\leftarrow$, right $\rightarrow$, top $\uparrow$, bottom $\downarrow$), until no further progress can be made. For every step $k$, the added area is recorded as the propagation flux $\delta A_k$:

$$\delta A_k = A_{k+1} - A_k \tag{1}$$

The propagation flux $\delta A$ in fact represent the infinitesimal areal addition in every step and can be used to separate any two aggregates from an appropriate necking points, since it identifies the weakly-connected zones, due to mis-identification.

### 3.2. Circularity (roundness) $C$

Since the physical appearance of each aggregate naturally has a rounded geometry to some extend, herein we use the roundness measure (i.e. circularity) $C$, defined as [75]:

$$C = 4\pi \frac{A}{P^2} \tag{2}$$

where $A$ is the area of the identified aggregate, and $P$ is its periphery. The roundness value is 1 for a perfect circle and is 0 for a line ($0 \leq C \leq 1$), which is used to avoid the excessively branched and porous identification of aggregates, shown in Fig. 2(a), since branching and porosity leads to smaller area with higher periphery (i.e. $A \downarrow$, $P \uparrow$).

### 3.3. Percolation framework

Herein, we use the percolation framework to estimate and separate the aggregates from each other, during the image processing as follows:

**1.** Each figure has been read into the three distinct red, green and blue matrix distributions $\{R, G, B\} \in [0, 255]$. Subsequently it has been converted to the gray-scale image by performing the appropriate coefficients $f$ from each sub-component image, as [76]:

$$f = \begin{bmatrix} 0.299 & 0.587 & 0.114 \end{bmatrix}$$

Then, the obtained gray-scale image is normalized to the maximum value to achieve the intensity value of: $I_{i,j} \in [0, 1]$.

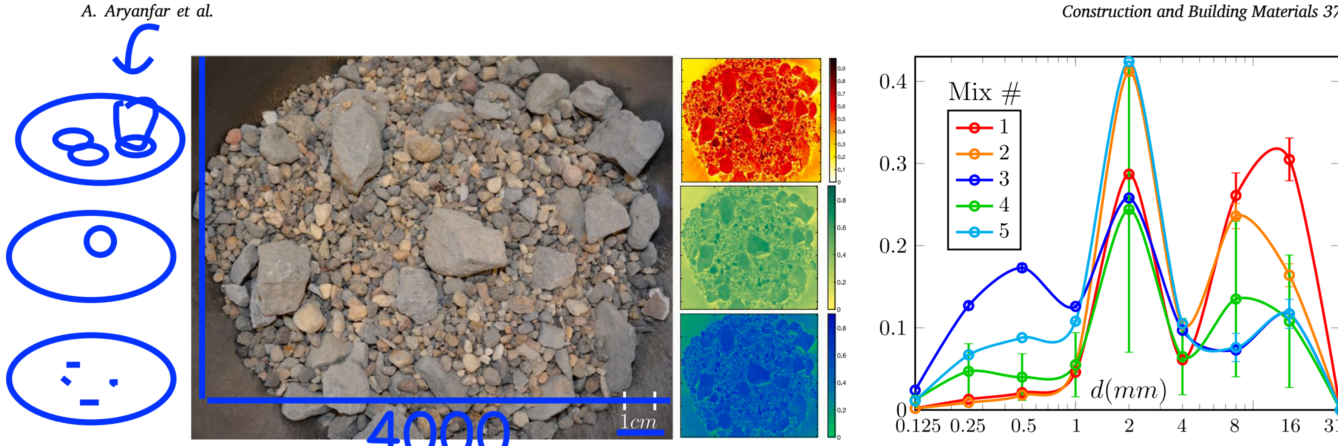


(a) Sample color image, illustrating the red, green, and blue intensity distributions. (b) Retained aggregated size distributions versus their respective sieve diameter $d$.

**Fig. 1.** Sample experiment from Sieve Analysis. (For interpretation of the references to color in this figure legend, the reader is referred to the web version of this article.)

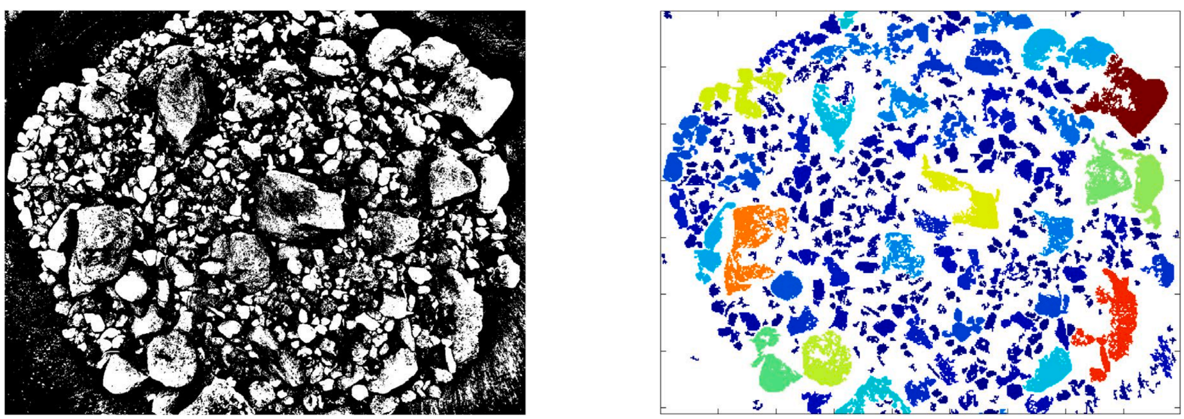

(a) Binarized Image obtained via adaptive thresholding. (b) Bare chain of aggregates obtained via percolation. The color spectrum commensurates with the area of the aggregates in increasing order from blue to red.

**Fig. 2.** The binarized image from Fig. 1(a) (left) and the initially-connected aggregate regions (right). (For interpretation of the references to color in this figure legend, the reader is referred to the web version of this article.)

**2.** Due to computational cost, the read image needs to be compressed down for performing an affordable evaluation. Hence, performing the scale-down by the compression factor of $\beta$, each $\beta$ number of pixels in the horizontal and vertical directions are grouped into an averaged single pixel.

**3.** The lower-resolution gay-scale image $I_{i,j}$ is binarized using adaptive thresholding that was originally introduced by Otsu [77] in the global scale. Hence, performing local thresholding through the group of 1st order neighbors for each pixel, the local grayness threshold $I_c$ determines the binarized value of $J_{i,j}$ for each pixel as the following [78]:

$$J_{i,j} = \begin{cases} 1 & I_{i,j} \geq I_c \\ 0 & I_{i,j} < I_c \end{cases} \tag{3}$$

Such local grayness threshold is attained via the minimization of the weighted intra-class variance $\sigma^2$ [74], defined proportionally as below:

$$\begin{cases} \sigma^2 = \omega_0\sigma_0^2 + \omega_1\sigma_1^2 \\ \omega_0 + \omega_1 = 1 \end{cases} \tag{4}$$

where $\omega_0$ and $\omega_1$ are the individual weight of each black (0) and white (1) portion as the fraction of total, and $\sigma_0^2$ and $\sigma_1^2$ are their respective variances. Such minimization ensures that either resulted black and white groups are selected from the most similar numbers in the closest proximity of each other. (i.e. closest ∼ lowest variance).

**4.** We track the propagation flux $\delta A_k$ by performing percolation in the connected clusters of the previous step to identify the points of weak connections (i.e. necks) which is unrealistic representation of the aggregates. The local minimization of percolation flux helps to identify such separation points, which could be extracted as:

$$\begin{aligned} &\text{Minimize} && \delta A_k = A_k - A_{k+1} \\ &\text{Such that} && A_k = \alpha^2\beta^2\left(\textstyle\sum 1\right)_k \end{aligned} \tag{5}$$

Mathematically the local minima is obtained as the locus where the slope changes sign, while maintaining the positive curvature, hence:

$$\begin{cases} \dfrac{\delta}{\delta k}\left(\delta A_k\right) \cdot \dfrac{\delta}{\delta k}\left(\delta A_{k+1}\right) < 0 & \text{Slope sign change} \\ \dfrac{\delta^2}{\delta k^2}\left(\delta A_k\right) > 0 & \text{Positive curvature} \end{cases} \tag{6}$$

Fig. 3 shows illustrate an example of connected aggregate cluster, where the individual aggregates are separated from the necks (dashed lines), by means of locating the local minima in the propagation flux, which is shown as the inset.

**5.** Performing the percolation on the each identified aggregate cluster $n$, we record the roundness $C_k$ at every percolation step $k$ as given in Eq. (2), as below:

$$\begin{aligned} &\text{Maximize} && C_k = 4\pi\frac{A_k}{P_k^2} \\ &\text{Such that} && A_k = \alpha^2\beta^2\left(\textstyle\sum 1\right)_k \quad , \quad P_k = \alpha\beta p_k \end{aligned} \tag{7}$$

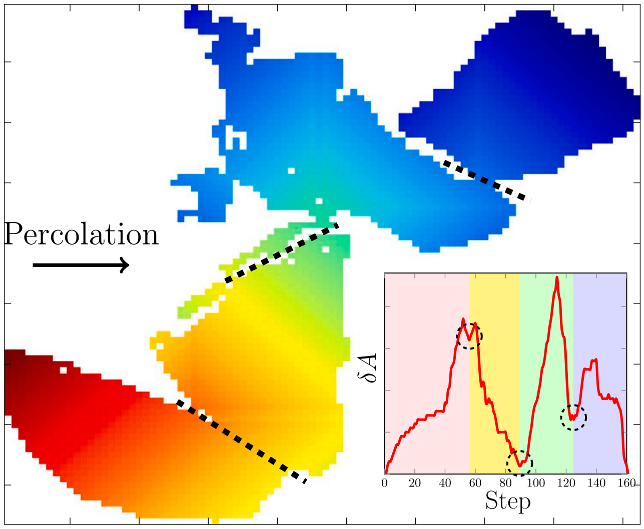


**Fig. 3.** Performing the sweeping percolation, and tracking the percolation flux $\delta A$, which is the added area in every step, it becomes locally small in the necks, which signifies the locus of weak connections. The local minima have been encircled in the subset.

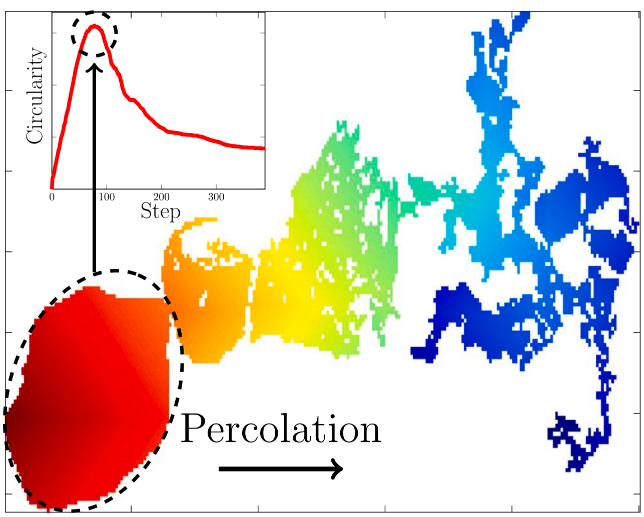


**Fig. 4.** Tracking the instantaneous circularity of the percolating region and locating the maximum of its circularity $C$ ensues the most rounded shape of the propagation, which is encircled in the subset.

where $A_k$ is the area, $P_k$ is the periphery of the growing cluster in the step $k$, $\alpha$ and $\beta$ are the calibration and compression factors and $p_k$ is the number of the pixels having less than 4 neighbors, ensuring that they are not fully surrounded and are part of periphery. Moving forward each new pixel is indexed in descending order, based on the step number. Fig. 4 shows an example of the tracking for the roundness, where its maximization leads to realistic identification of the aggregate from the rest of the identified cluster. Hence the cluster with the maximum roundness is extracted out.

**6.** Repeat the steps 4 and 5 until no white pixel remains in the aggregate chain $n$.

**7.** The equivalent diameter $d_{Eq}$ of each individual aggregate by presuming the obtained area$A$ as a circle, where $d_{Eq} := \left(\frac{4A}{\pi}\right)^{\frac{1}{2}}$.

Figs. 5 and 6 show the compressed low resolution original images, the respective binarized image and the processed image with the extracted aggregates which are color-coded based on the respective areas.

## 4. Results & discussions

The methodology for extracting the aggregates works on the series steps in multitudes of scales. Starting from the scale of entire domain, the extent of connected aggregate chains are initially identified. Subsequently an intermediate-scale sweeping percolation is performed where the propagation flux is traced and its respective local minima signifies the locus of weak connections (i.e. necks). Consequently, the aggregate-scale sweeping percolation is carried out where tracking the instantaneous circularity of the growing cluster and identification of the locus of maximum roundness ensures extracting the most natural shape of the aggregates. Such larger-to-smaller scale analysis for a aggregates chain has been visualized in Fig. 8.

The comparison of the trends of aggregate size histograms presented in Fig. 7 shows that the higher resolution, which corresponds to lower compression factor $\beta$ from the original image, provides a closer correlation with the experimental diameter distributions. In fact comparing the diameter fraction in the experiments $f_{EXP}$ and the computations $f_i$, one can define the error sum Err as the addition in the magnitude of their differences as:

$$\mathrm{Err} = \sum_{i=1}^{n} |f_i - f_{EXP,i}| \tag{8}$$

Therefore:

$$\beta \uparrow \Rightarrow \mathrm{Err} \downarrow \tag{9}$$

As an example, the experimental histograms of the Sample 5 is compared against the histograms obtained in our framework as well as Otsu's method for 3 resolutions in Fig. 9. Visually, the error sum Err in the histograms translates into the distance between the peaks, where the closer the experimental and computational peaks, the more accurate the histogram approximation. Since the optimization due to minimizing the propagation flux $\delta A$ and maximizing the circularity $C$ divides the larger identified clusters to smaller ones, as illustrated in Figs. 3 and 4, we observe in this that such error is significantly reduced in our computations, versus the traditional Otsu's method.

Additionally, due to decomposition of the larger aggregates to the smaller one with variety of the equivalent diameters, it is observed that the distribution from the established framework has a wider distribution, as opposed to the spike-like histogram obtained from the Otsu's method, which is in more agreement with the experimental findings.

Moreover, the established framework contains advantages relative to the ImageJ software since imageJ is limited to the assumption of the elliptic shapes and does not capture the other geometries, while the current percolation-based method can capture the aggregates with sharp corners and finer details.

Consequently, the $2D$ (image) results from the simulations $3D$ (real) results from the experiments correlate with the diameters as follows by dimensional analysis:

$$A \propto d^2 \quad , \quad V \propto d^3 \tag{10}$$

therefore, one can obtain the areal and volumetric distributions from the diameter. Since the histogram fractions are less than one ($f_i < 1$) applying higher powers will shrink the values, and such shrinkage is the highest for the volumetric distribution than the areal counterpart. This is already observable from the histograms in Fig. 7, as the experimental distributions are wider and in some cases contain more than one peaks. As well the peaks in the volumetric distributions should be shorter than the areal version, which is already observable from the obtained histograms in this Figure.

Finally, it should be mentioned that imposing the compression factor of $\beta$ uses only $\sim 1/\beta^2$ information from the original image (*i.e.* only 1% of image information for $\beta = 10$), hence the projected grain size distributions is deemed appropriate. Henceforth, we ascribe that developed percolation-based computation particularly useful as a fast tool for obtaining the peak of the histograms, containing the dominant diameter $d_{EFF}$ containing the maximum fraction. ($f_{max}, d_{EFF}$), as the wholistic size measure.

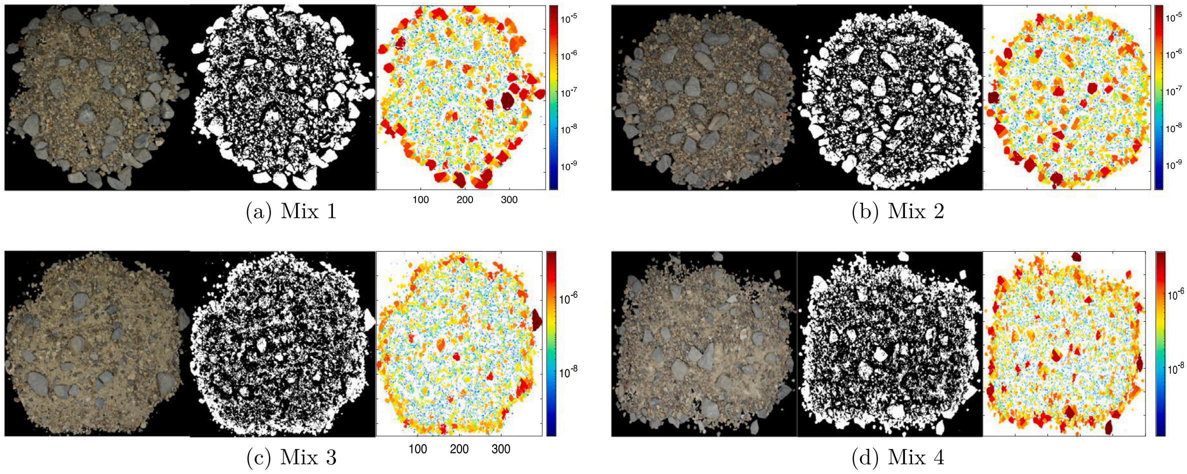


**Fig. 5.** Aggregate extraction for 4 samples with the compression factor of $\beta = 10$ (1/100 resolution), containing $\sim 400^2$ pixels. The first, second and third image in each processing corresponds to the bare compressed image, locally-binarized image and the extracted aggregates distribution, where the color range from blue to red corresponds the aggregated area. (For interpretation of the references to color in this figure legend, the reader is referred to the web version of this article.)

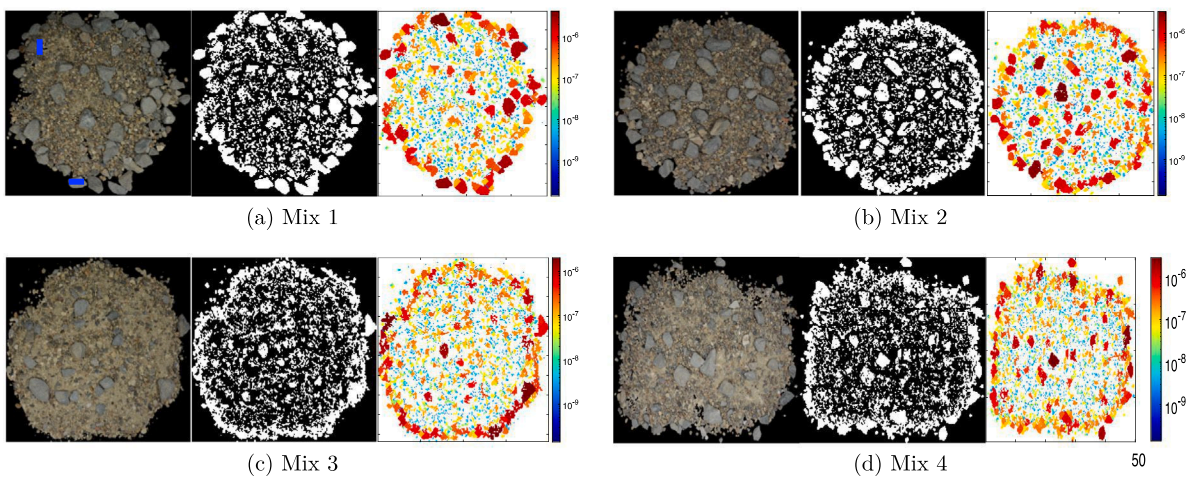


**Fig. 6.** Aggregate extraction for 4 samples with the compression factor of $\beta = 20$ (1/400 resolution), containing $\sim 200^2$ pixels. The first, second and third image in each processing corresponds to the bare compressed image, locally-binarized image and the extracted aggregates distribution, where the color range from blue to red corresponds the aggregated area. (For interpretation of the references to color in this figure legend, the reader is referred to the web version of this article.)

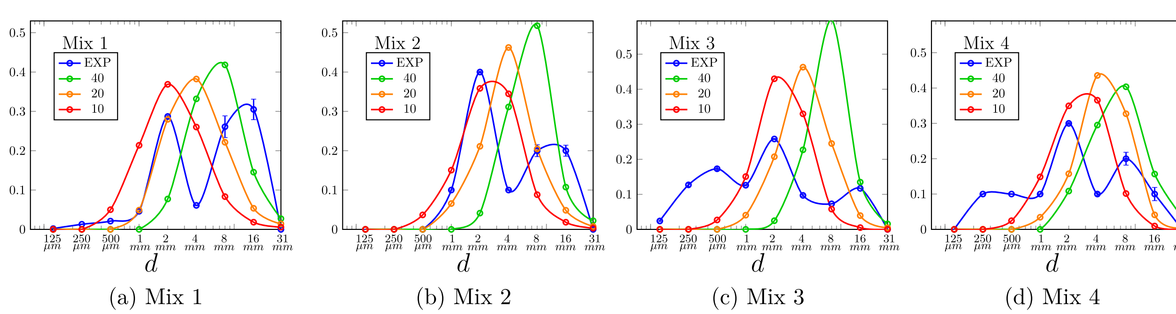


**Fig. 7.** The distributions of the retained aggregates versus the resolution for 4 samples, compared with their respective experimental sieve analysis.

## 5. Conclusions

In this paper, a new method has been developed for obtaining the size distributions of the aggregates from the experimental images. The framework initially proceeds via binarization and resizing of the experimental image. Subsequently percolation has been performed through the aggregate networks to identify the maximum coverage of the connected clusters, where no further percolation is possible. Subsequently another round of percolation has been run on the connected islands, where the locus of weak attachment (i.e. necks), where identified via tracking the local minima in the propagation flux. Consequently, in order to realistically capture the mainly rounded and convex shape of the individual aggregates, the last round of percolation has been performed in local scale for maximizing the circularity of the propagation. The obtained histograms have been compared/verified with our experimental measurements, the correlation with the compression factor has been analyzed, and the advantages to other image processing frameworks such as ImageJ and Otsu's method have been conveyed.

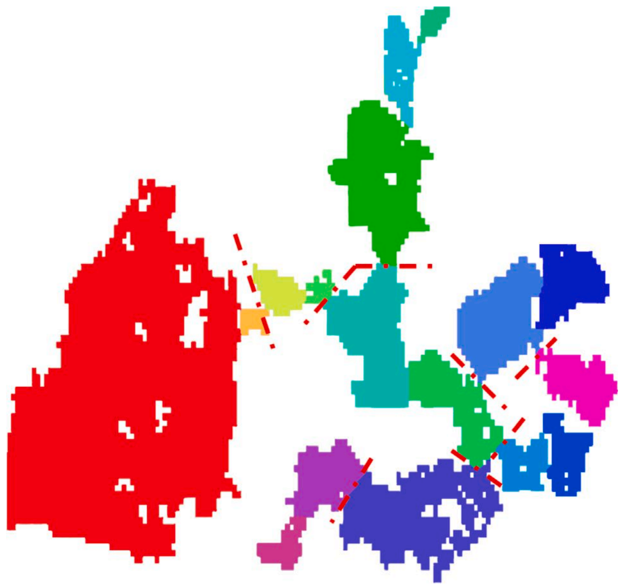

**Fig. 8.** Schematics of how minimization of flux $\delta A$ identifies the weakly connected regions (dashed lines) and maximizing the circularity $C$ of the sub-regions (colored) extracts out the closest proximity to the natural shape of grains.

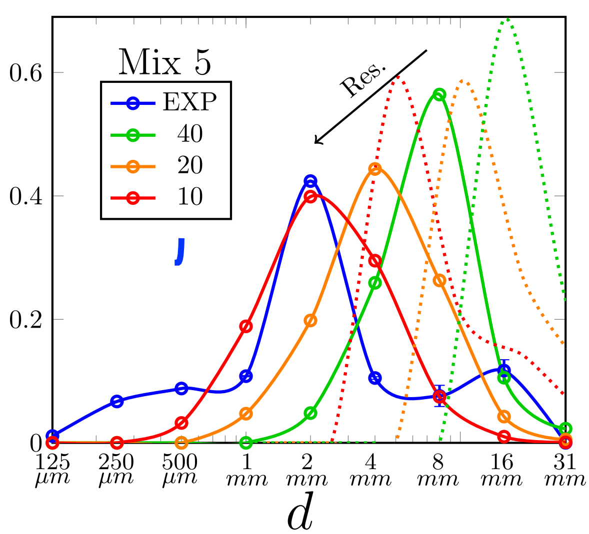


**Fig. 9.** The correlation of the experimental measurements (blue) with the obtained charts of different resolutions (solid) and the Otsu's method (dashed), illustrating the effect of the resolution. (For interpretation of the references to color in this figure legend, the reader is referred to the web version of this article.)

The established framework could be useful for the on-site and realistic estimation of the aggregate distributions, particularly those of unusual geometries with sharp peripheries.

## List of symbols

| | |
|---|---|
| $\alpha$ | Experimental calibration factor (m/pixels). |
| $\beta$ | Computational Resize factor. |
| $A$ | Area of the aggregate. |
| $P$ | Perimeter of the aggregate. |
| $p$ | peripheral pixels |
| $d$ | Calculated diameter of the aggregate |
| $m$ | Mass of the aggregate |
| $V$ | Volume of the aggregate. |
| $\sigma$ | Variance based on Otsu's method. |
| $\sigma_0$ | variance of white pixels |
| $I_{i,j}$ | Normalized intensity image. |
| $FM$ | fineness modulus. |
| Err | Error sum |
| $f_i$ | fraction of $d_i$ in the simulations |
| $f_{EXP}$ | fraction of $d_i$ in the experiments |
| $\sigma_1$ | variance of black pixels |
| $\omega_0$ | fraction of white pixels |
| $\omega_1$ | fraction of black pixels |
| $C$ | Roundness (Circularity) |
| $\delta A$ | Propagation flux |
| $N$ | Number of aggregates found |
| $J_{i,j}$ | Binarized image. |

## CRediT authorship contribution statement

**Asghar Aryanfar:** Conceptualization, Validation, Formal analysis, Investigation, Data curation, Writing – original draft, Writing – review & editing, Visualization, Funding acquisition. **Maria N. Khoury:** Methodology, Resources, Software, Writing – review & editing, Supervision, Project administration. **Irem Şanal:** Consultation & Supervision. **Dana Şeyhibrahim:** Experimental data acquisition, Data curation. **Jaime Marian:** Project administration.

## Declaration of competing interest

The authors declare that they have no known competing financial interests or personal relationships that could have appeared to influence the work reported in this paper.

## Data availability

Data will be made available on request.

## Acknowledgments

This work has been financially supported by the Scientific Research Project Coordination Center of Bahçeşehir University Project No. BAP.2020.01.12. The authors would like to thank the support from the Masri Institute from American University of Beirut, Grant Award No. 103919 for the student Maria Khoury.

## Appendix A. Supplementary data

Supplementary material related to this article can be found online at https://doi.org/10.1016/j.conbuildmat.2023.131109.

## References

[1] E. Amézketa, Soil aggregate stability: a review, J. Sustain. Agric. 14 (2–3) (1999) 83–151.
[2] Vivian WY Tam, Harshana Wattage, Khoa N Le, Anthony Buteraa, Mahfooz Soomro, Methods to improve microstructural properties of recycled concrete aggregate: A critical review, Constr. Build. Mater. 270 (2021) 121490.
[3] Senthil Kumar Kaliyavaradhan, Tung-Chai Ling, Kim Hung Mo, Valorization of waste powders from cement-concrete life cycle: A pathway to circular future, J. Clean. Prod. 268 (2020) 122358.
[4] Payam Shafigh, Hilmi Bin Mahmud, Mohd Zamin Jumaat, Majid Zargar, Agricultural wastes as aggregate in concrete mixtures–A review, Constr. Build. Mater. 53 (2014) 110–117.
[5] Mohamadreza Moini, Ismael Flores-Vivian, Adil Amirjanov, Konstantin Sobolev, The optimization of aggregate blends for sustainable low cement concrete, Constr. Build. Mater. 93 (2015) 627–634.
[6] Subha Ghosh, Nirjhar Dhang, Arghya Deb, Influence of aggregate geometry and material fabric on tensile cracking in concrete, Eng. Fract. Mech. 239 (2020) 107321.
[7] P.K. Mehta, PJM Monteiro, Concrete: Structure, Properties and Materials, Prentice Hall Inc., Englewood Cliffs, NJ, 1993, p. 548.

[8] Sidney Mindess, J. Francis Young, David Darwin, Concrete, Vol. 481, Prentice-Hall, Englewood Cliffs, NJ, 1981.
[9] Steven H Kosmatka, Beatrix Kerkhoff, William C Panarese, et al., Design and Control of Concrete Mixtures, vol. 5420, Portland Cement Association Skokie, IL, 2002.
[10] Xingwang Wang, Hainian Wang, Ponan Feng, Chonghui Wang, Chen Zhang, Amir Golroo, The movement property characterization of coarse aggregate during gyratory compaction based on 3D-printed aggregate, Constr. Build. Mater. 361 (2022) 129608.
[11] Jerzy Wawrzeńczyk, Agnieszka Molendowska, The use of a special stereoscopic microscope attachment for the sieve analysis of aggregate in concrete, Appl. Sci. 9 (9) (2019) 1853.
[12] M. Abdullahi, Effect of aggregate type on compressive strength of concrete, Int. J. Civ. Struct. Eng. 2 (3) (2012) 791–800.
[13] Ante Jadrijević, Wet sieve analysis of fresh concrete correction procedures, Cem. Concr. Res. 23 (6) (1993) 1307–1316.
[14] Emanuel Azmon, Field method for sieve analysis of sand, J. Sediment. Res. 31 (4) (1961) 631–633.
[15] Fátima Cristina Lira, Pedro Pina, Grain size measurement in images of sands, in: VISAPP (1), 2006, pp. 371–374.
[16] Eric Pirard, Nicolas Vergara, Vincent Chapeau, Direct estimation of sieve size distributions from 2-D image analysis of sand particles, in: Proceedings PARTEC 2004, 2004.
[17] Joanne M.R. Fernlund, The effect of particle form on sieve analysis: a test by image analysis, Eng. Geol. 50 (1–2) (1998) 111–124.
[18] Štefánia Olejárová, Juraj Ružbarskỳ, Tibor Krenickỳ, Sieve analysis, in: Vibrations in the Production System, Springer, 2019, pp. 15–28.
[19] Taleb Al-Rousan, Eyad Masad, Erol Tutumluer, Tongyan Pan, Evaluation of image analysis techniques for quantifying aggregate shape characteristics, Constr. Build. Mater. 21 (5) (2007) 978–990.
[20] Nicoletta Marinoni, Alessandro Pavese, Marco Foi, Luca Trombino, Characterisation of mortar morphology in thin sections by digital image processing, Cem. Concr. Res. 35 (8) (2005) 1613–1619.
[21] Zhong Qi Yue, Isabelle Morin, Digital image processing for aggregate orientation in asphalt concrete mixtures, Can. J. Civil Eng. 23 (2) (1996) 480–489.
[22] Michel Coster, Jean-Louis Chermant, Image analysis and mathematical morphology for civil engineering materials, Cem. Concr. Compos. 23 (2–3) (2001) 133–151.
[23] Krzysztof Ostrowski, Damian Stefaniuk, Łukasz Sadowski, Kamil Krzywiński, Magdalena Gicala, Magdalena Różańska, Potential use of granite waste sourced from rock processing for the application as coarse aggregate in high-performance self-compacting concrete, Constr. Build. Mater. 238 (2020) 117794.
[24] Anna-Lena Persson, Image analysis of shape and size of fine aggregates, Eng. Geol. 50 (1–2) (1998) 177–186.
[25] Junyao Tang, Yongqiang Fu, Tao Ma, Binshuang Zheng, Yao Zhang, Xiaoming Huang, Investigation on low-temperature cracking characteristics of asphalt mixtures: A virtual thermal stress restrained specimen test approach, Constr. Build. Mater. 347 (2022) 128541.
[26] Albert K.H. Kwan, C.F. Mora, H.C. Chan, Particle shape analysis of coarse aggregate using digital image processing, Cem. Concr. Res. 29 (9) (1999) 1403–1410.
[27] C.F. Mora, A.K.H. Kwan, H.C. Chan, Particle size distribution analysis of coarse aggregate using digital image processing, Cem. Concr. Res. 28 (6) (1998) 921–932.
[28] GHAJJ Kumara, K. Hayano, K. Ogiwara, Fundamental study on particle size distribution of coarse materials by image analysis, in: First International Conference on Geotechnique, Construction Materials and Environment, 2011, pp. 399–404.
[29] Larry Banta, Ken Cheng, John Zaniewski, Estimation of limestone particle mass from 2D images, Powder Technol. 132 (2–3) (2003) 184–189.
[30] Joanne M.R. Fernlund, Robert W. Zimmerman, Danica Kragic, Influence of volume/mass on grain-size curves and conversion of image-analysis size to sieve size, Eng. Geol. 90 (3–4) (2007) 124–137.
[31] Mitra Mosharraf, Christer Nyström, The effect of particle size and shape on the surface specific dissolution rate of microsized practically insoluble drugs, Int. J. Pharm. 122 (1–2) (1995) 35–47.
[32] Prashanth Vangla, Nimisha Roy, Kavya Mendu, Gali Madhavi Latha, Digital image analysis for the determination of size and shape parameters of sand grains, in: Golden Jubilee Conference of the IGS Bangalore Chapter Geo-Innovations, 2014, pp. 1–9.
[33] Nattaporn Prakongkep, Anchalee Suddhiprakarn, Irb Kheoruenromne, Robert J Gilkes, SEM image analysis for characterization of sand grains in Thai paddy soils, Geoderma 156 (1–2) (2010) 20–31.
[34] GHAJJ Kumara, Kimitoshi Hayano, Keita Ogiwara, Image analysis techniques on evaluation of particle size distribution of gravel, Int. J. Geomate 3 (1) (2012) 290–297.
[35] Chun-Yi Kuo, Reed B. Freeman, Imaging indices for quantification of shape, angularity, and surface texture of aggregates, Transp. Res. Rec. 1721 (1) (2000) 57–65.
[36] F. Altuhafi, C.O. sullivan, I. Cavarretta, Analysis of an image-based method to quantify the size and shape of sand particles, J. Geotech. Geoenviron. Eng. 139 (8) (2013) 1290–1307.
[37] Hakon Wadell, Volume, shape, and roundness of quartz particles, J. Geol. 43 (3) (1935) 250–280.
[38] Robert Louis Folk, Student operator error in determination of roundness, sphericity, and grain size, J. Sediment. Res. 25 (4) (1955) 297–301.
[39] C Igathinathane, LO Pordesimo, EP Columbus, WD Batchelor, SR Methuku, Shape identification and particles size distribution from basic shape parameters using imagej, Comput. Electron. Agric. 63 (2) (2008) 168–182.
[40] Jurjen Broeke, José María Mateos Pérez, Javier Pascau, Image Processing with ImageJ, Packt Publishing Ltd, 2015.
[41] Bethany C Winstone, Richard J Heck, Lars J Munkholm, Bill Deen, Characterization of soil aggregate structure by virtual erosion of X-ray CT imagery, Soil Tillage Res. 185 (2019) 70–76.
[42] Solomon Tafesse, J.M.R. Fernlund, Fredrik Bergholm, Digital sieving-matlab based 3-D image analysis, Eng. Geol. 137 (2012) 74–84.
[43] Junqing Zhu, Tao Ma, Zhen Dong, Evaluation of optimum mixing conditions for rubberized asphalt mixture containing reclaimed asphalt pavement, Constr. Build. Mater. 234 (2020) 117426.
[44] C. Shanthi, R. Kingsley Porpatham, N. Pappa, Image analysis for particle size distribution, Int. J. Eng. Technol. 6 (3) (2014) 1340–1345.
[45] Leonardo Bruno, Giuseppe Parla, Clara Celauro, Image analysis for detecting aggregate gradation in asphalt mixture from planar images, Constr. Build. Mater. 28 (1) (2012) 21–30.
[46] C.F. Mora, AKH Kwan, Sphericity, shape factor, and convexity measurement of coarse aggregate for concrete using digital image processing, Cem. Concr. Res. 30 (3) (2000) 351–358.
[47] Murat Ozen, Murat Guler, Assessment of optimum threshold and particle shape parameter for the image analysis of aggregate size distribution of concrete sections, Opt. Lasers Eng. 53 (2014) 122–132.
[48] Thae Nu Wah, Pann Ei San, Thandar Hlaing, Analysis on feature extraction and classification of rice kernels for Myanmar rice using image processing techniques, Int. J. Sci. Res. Publ. 8 (8) (2018) 603–606.
[49] Wei Wu, Tao Liu, Ping Zhou, Tianle Yang, Chunyan Li, Xiaochun Zhong, Chengming Sun, Shengping Liu, Wenshan Guo, Image analysis-based recognition and quantification of grain number per panicle in rice, Plant Methods 15 (1) (2019) 1–14.
[50] Sachin B. Jadhav, Sanjay B. Patil, Grading of soybean leaf disease based on segmented image using k-means clustering, Int. J. Adv. Res. Electr. Commun. Eng. 4 (6) (2015) 1816–1822.
[51] Pendar Alirezazadeh, Fatemeh Rahimi-Ajdadi, Yousef Abbaspour-Gilandeh, Niels Landwehr, Hamed Tavakoli, Improved digital image-based assessment of soil aggregate size by applying convolutional neural networks, Comput. Electron. Agric. 191 (2021) 106499.
[52] Allen Hunt, Robert Ewing, Behzad Ghanbarian, Percolation Theory for Flow in Porous Media, Vol. 880, Springer, 2014.
[53] M. Yanuka, Percolation theory approach to transport phenomena in porous media, Transp. Porous Media 7 (3) (1992) 265–282.
[54] Haralampos Zois, Lazaros Apekis, Yevgen P. Mamunya, Dielectric properties and morphology of polymer composites filled with dispersed iron, J. Appl. Polym. Sci. 88 (13) (2003) 3013–3020.
[55] Y. Shim, L.E. Levine, R.J. Fields, Optimal concentration of SiC in SiC/Al composites: experiment and percolation theory prediction of lower and upper bounds, Physica A 348 (2005) 1–15.
[56] Roey Nadiv, Michael Shtein, Gal Shachar, Maxim Varenik, Oren Regev, Optimal nanomaterial concentration: harnessing percolation theory to enhance polymer nanocomposite performance, Nanotechnology 28 (30) (2017) 305701.
[57] G.A. Gist, A.H. Thompson, A.J. Katz, R.L. Higgins, Hydrodynamic dispersion and pore geometry in consolidated rock, Phys. Fluids A 2 (9) (1990) 1533–1544.
[58] M. Sahimi, Hydrodynamic dispersion near the percolation threshold: Scaling and probability densities, J. Phys. A: Math. Gen. 20 (18) (1987) L1293.
[59] Łukasz Kulacz, Adrian Kliks, Reliability assessment of bio-inspired ultra-dense networks using percolation theory, in: 2020 IEEE 21st International Symposium on "A World of Wireless, Mobile and Multimedia Networks", WoWMoM, IEEE, 2020, pp. 173–175.
[60] Michael Aizenman, Charles M. Newman, Tree graph inequalities and critical behavior in percolation models, J. Stat. Phys. 36 (1) (1984) 107–143.
[61] Russell Lyons, Random walks, capacity and percolation on trees, Ann. Probab. (1992) 2043–2088.
[62] József Balogh, Yuval Peres, Gábor Pete, Bootstrap percolation on infinite trees and non-amenable groups, Combin. Probab. Comput. 15 (5) (2006) 715–730.
[63] Paul N. Suding, Robert M. Ziff, Site percolation thresholds for archimedean lattices, Phys. Rev. E 60 (1) (1999) 275.
[64] Fumiko Yonezawa, Shoichi Sakamoto, Motoo Hori, Percolation in two-dimensional lattices. I. A technique for the estimation of thresholds, Phys. Rev. B 40 (1) (1989) 636.
[65] Ying Chen, Christopher A. Schuh, Diffusion on grain boundary networks: Percolation theory and effective medium approximations, Acta Mater. 54 (18) (2006) 4709–4720.
[66] Y.B. Yi, E. Tawerghi, Geometric percolation thresholds of interpenetrating plates in three-dimensional space, Phys. Rev. E 79 (4) (2009) 041134.

[67] Jianjun Lin, Huisu Chen, Wenxiang Xu, Geometrical percolation threshold of congruent cuboidlike particles in overlapping particle systems, Phys. Rev. E 98 (1) (2018) 012134.
[68] D. Stauffer, A. Aharony, INtroduction to Percolation Theory, Vol. 96, Taylor & Francis, London, Washington, DC, 1992.
[69] Igor'M Sokolov, Dimensionalities and other geometric critical exponents in percolation theory, Sov. Phys. Uspekhi 29 (10) (1986) 924.
[70] H.-P. Hsu, M.-C. Huang, Percolation thresholds, critical exponents, and scaling functions on planar random lattices and their duals, Phys. Rev. E 60 (6) (1999) 6361.
[71] O. Melchert, Percolation thresholds on planar Euclidean relative-neighborhood graphs, Phys. Rev. E 87 (4) (2013) 042106.
[72] Christian R. Scullard, Exact site percolation thresholds using a site-to-bond transformation and the star-triangle transformation, Phys. Rev. E 73 (1) (2006) 016107.
[73] ČSN EN, et al., Tests for geometrical properties of aggregates–Part 1: Determination of particle size distribution–sieving method, 2012.
[74] Derek Bradley, Gerhard Roth, Adaptive thresholding using the integral image, J. Graph. Tools 12 (2) (2007) 13–21.
[75] Yasuhiro Takashimizu, Maiko Iiyoshi, New parameter of roundness R: circularity corrected by aspect ratio, Prog. Earth Planet. Sci. 3 (1) (2016) 1–16.
[76] Min Qiu, Graham D. Finlayson, Guoping Qiu, Contrast maximizing and brightness preserving color to grayscale image conversion, in: Conference on Colour in Graphics, Imaging, and Vision, Vol. 2008, Society for Imaging Science and Technology, 2008, pp. 347–351.
[77] Nobuyuki Otsu, A threshold selection method from gray-level histograms, Automatica 11 (285–296) (1975) 23–27.
[78] Asghar Aryanfar, Michael R. Hoffmann, William A. Goddard III, Finite-pulse waves for efficient suppression of evolving mesoscale dendrites in rechargeable batteries, Phys. Rev. E 100 (4) (2019) 042801.